J. Fluid Mech. (2004), *vol.* 508, *pp.* 265–286.
DOI: 10.1017/S0022112004009255 Printed in the United Kingdom

Amplitude equilibration of sugar–salt fingers

By MELVIN E. STERN AND JULIAN SIMEONOV

Department of Oceanography, Florida State University, Tallahassee, FL 32306-4320, USA
stern@ocean.fsu.edu

(Received 7 August 2003 and in revised form 29 January 2004)

The mechanism by which amplifying salt fingers in an unbounded uniform T/S gradient are equilibrated is determined, starting with a time-dependent asymptotic field equation for $(R\tau)^{-1} - 1 = \varepsilon \to 0$, where $R > 1$ is the T/S density ratio and $\tau = K_S/K_T < 1$ is the molecular diffusivity ratio. A mode truncation of that equation yields an ODE which shows that the fastest growing finger mode transfers energy to two 'slave' modes with relatively small vertical scale; the finger mode thereby attains a statistically steady amplitude. The results for $\tau = 1/3$ are compared with spectral solutions of the non-truncated equations in two and three dimensions; the predicted fluxes are testable in sugar (S), salt (T) laboratory experiments.

1. Introduction

A doubly diffusive fluid consists of two different substances (T, S) with molecular diffusivities $K_T > K_S$. In an unbounded basic state with uniform vertical gradients ($\overline{T}_z$, $\overline{S}_z$) and a density ratio R:

$$1 < R \equiv \overline{T}_z/\overline{S}_z < K_T/K_S \equiv 1/\tau, \tag{1.1}$$

the primary instability consists of long thin salt fingers (see Kunze 2003 for a review of salt fingers). Here and in all that follows the (constant) coefficients of expansion are absorbed in the T, S symbols so that these represent the density contributions to the linear equation of state in the Boussinesq dynamics.

There are several previous numerical and qualitative studies (see Shen 1995 and Stern, Radko & Simeonov 2001, for example) of the statistical equilibration of fingers in the case of oceanographic interest, wherein T = temperature, S = salinity, and

$$\frac{1}{R\tau} - 1 \equiv \varepsilon \tag{1.2}$$

is large ($\varepsilon \gg 1$). Shen (1995) demonstrates that the originally z-independent fingers equilibrate due to Holyer's (1984) instability, in which the new unstable mode corresponds to a vertically periodic horizontal shear flow. As the latter amplifies, the straight fingers become wavy and eventually break apart into a disorganized convection of rising and sinking blobs. A qualitatively different picture is often found in laboratory sugar–salt experiments where the distorted equilibrium fingers retain their vertical coherence and relative organization (e.g. figure 4 of Krishnamurti 2003). We note that in the limit of large Prandtl number the growth rate of Holyer's (1984, her equation (4.35)) shear flow instability approaches zero, so that there must be a different instability/equilibration mechanism. Here we seek such an alternative mechanism for the equilibration of sugar–salt fingers, and we shall consider the question in a tractable

regime wherein

$$\varepsilon \to 0^+. \tag{1.3}$$

Unlike Holyer (1984), who considers the stability of steady finite-amplitude fingers, in the present study the basic state will correspond to the fastest growing fingers. This regime is experimentally realizable with a uniform salt(T)/sugar(S) gradient produced in a tall vessel using the 'double-bucket' technique (see Stern & Turner 1969).

Nonlinear evolutionary equations applicable to this limit (1.3) were obtained (Radko & Stern 1999) by making an asymptotic expansion of the high-Prandtl-number (ν/K_T) equations appropriate to sugar–salt. For the convenience of the reader the derivation of these equations will be reviewed in § 2. It is noteworthy that in these $\varepsilon \ll 1$ equations there is negligible modification of the mean $\overline{T}_z$, $\overline{S}_z$ field by the fingers, and therefore equilibration of this field is only possible by nonlinear modal (triad) interactions. To explore this mechanism the two-dimensional version of the Radko–Stern equation will be truncated (§ 3) to obtain the interaction of the long thin primary finger mode with two 'slave' modes characterized by negative growth rate in the linearized primary instability theory. After showing (§ 3) that these small disturbances grow at the expense of the long finger mode, we turn to the steady solutions of the governing nonlinear ODE. These possible solutions are highly degenerate with respect to the permissible vertical wavenumber of the 'slaves'. Next (§ 3), the transient solution of the time-dependent ODE indicates that the aforementioned steady solutions are also unstable, and the statistically steady equilibrating triads are still highly degenerate. This point focuses attention on the question of which solution is realized in full two- and three-dimensional spectral calculations (§ 4 and § 5). The behaviour of these will be partially explained by the mode truncation theory in § 3. Additional statistics are obtained and summarized in § 6.

2. The $\varepsilon \to 0$ theory

The high-Prandtl-number equations

Since the sugar–salt Prandtl number is $\sim 10^3$, and

$$\tau \cong 1/3, \tag{2.1}$$

it is permissible to neglect the acceleration terms in the Boussinesq equations, while retaining the full T/S conservation equations. (It is assumed that for $R > 1$ the system will yield a solution with a moderate Reynolds number, consistent with the high-Prandtl-number equations.) These equations are now conventionally non-dimensionalized using a (finger) length scale

$$d \equiv (K_T \nu / g \overline{T}_z)^{1/4}, \tag{2.2}$$

a time scale d^2/K_T, a velocity scale K_T/d, a pressure scale $\nu K_T/d^2$, and $\overline{T}_z d$ as the scale for the total deviations ($T \equiv T' + \theta(z,t)$, $S \equiv S' + \sigma$) from the basic state ($\overline{T}(z)$, $\overline{S}(z)$). With $S' - T'$ as the density perturbation, and with periodic boundary conditions, the high-Prandtl-number equations are

$$0 = -\nabla p + \nabla^2 \boldsymbol{v} + (T' - S')\boldsymbol{k}, \tag{2.3a}$$

$$\nabla \cdot \boldsymbol{v} = 0, \tag{2.3b}$$

$$\frac{\mathrm{d}}{\mathrm{d}t}[T' + \theta] + w = \nabla^2 (T' + \theta), \quad \overline{T}' = 0 = \overline{S}' = \overline{w}, \tag{2.3c}$$

$$\frac{\mathrm{d}}{\mathrm{d}t}[S' + \sigma] + \frac{1}{R} w = \tau \nabla^2 (S' + \sigma), \quad \langle \theta \rangle = 0 = \langle \sigma \rangle, \tag{2.3d}$$

where the overbar and angle brackets denote horizontal and vertical average, respectively. The well-known fastest growing linear solution of these is independent of z, and has an x-wavelength $\sim d$.

$$\varepsilon \equiv (1/R\tau) - 1 \to 0 \text{ (Radko \& Stern 1999)}$$

In this next asymptotic expansion the choice of the x, y, t scales (equation (2.4)) in the new non-dimensionalization is motivated by the fact that these give the fastest growing finger mode in the linearization of (2.3) when $\varepsilon \to 0$. In addition, and most significantly, for the x-scale in (2.4) the largest vertical wavenumber that can be linearly amplified is given by the z-scaling in (2.4). Thus we substitute

$$x = \varepsilon^{-1/4} x_0, \quad y = \varepsilon^{-1/4} y_0, \quad z = \varepsilon^{-1/4} z_0, \quad t = \varepsilon^{-3/2} t_0, \tag{2.4}$$

$$(u, v, w) = \varepsilon^{5/4}(u_0, v_0, w_0) + \cdots, \quad p = \varepsilon^{3/2} p_0, \tag{2.5}$$

$$T = \varepsilon^{3/4} T_0 + \cdots, \quad S = \varepsilon^{3/4} S_0 + \cdots. \tag{2.6}$$

into (2.3) and then let $\varepsilon \to 0$. The scaling in (2.6) may be rationalized if it is anticipated that the density deviation $(S' - T')$ is smaller than the individual S' or T'. Dividing (2.3d) by τ, subtracting (2.3c) from the result, and neglecting the density diffusion term gives the following balance:

$$w\left(\frac{1}{\tau R} - 1\right) \sim w\frac{\partial T'}{\partial z} - \frac{w}{\tau}\frac{\partial S'}{\partial z} \sim \frac{wT'}{\varepsilon^{-1/4}}$$

or $T' \sim \varepsilon^{3/4}$. The diffusive advective balance $w \sim \nabla^2 T'$ then gives the velocity scale in (2.5), and the pressure scale follows from the horizontal momentum equation. In terms of the new coordinates with subscript zero the leading order $\varepsilon^{5/4}$ balance of both advection–diffusion equations yields the diagnostic equations

$$w_0 = \nabla_0^2 T_0 = \nabla_0^2 S_0, \tag{2.7}$$

thereby justifying

$$T_0 = S_0 \tag{2.8}$$

and

$$\overline{T}_0 = \overline{S}_0 = 0. \tag{2.9}$$

The pressure force in the vertical momentum equation requires the buoyancy force to be $O(\varepsilon^{7/4})$, and thus the T–S expansions should be continued as

$$T = \varepsilon^{3/4} T_0 + \varepsilon^{7/4} T_1, \quad S = \varepsilon^{3/4} S_0 + \varepsilon^{7/4} S_1, \quad w = \varepsilon^{5/4} w_0 + \varepsilon^{\overline{q}} w_1, \tag{2.10}$$

where $\overline{q}$ is an as yet undetermined exponent. (Since the $\overline{q}$ terms will cancel in the final result (2.16) it will not be necessary to determine $\overline{q}$.) The leading-order momentum equations are

$$\frac{\partial}{\partial x_0} p_0 = \nabla_0^2 u_0, \quad \frac{\partial}{\partial y_0} p_0 = \nabla_0^2 v_0, \tag{2.11}$$

$$\frac{\partial}{\partial z_0} p_0 = \nabla_0^2 w_0 + T_1 - \overline{T}_1 - (S_1 - \overline{S}_1). \tag{2.12}$$

After (2.7) the next order ($\varepsilon^{9/4}$) balance of the advection diffusion equation, using

$1/R = \tau(1+\varepsilon)$ and $q = \overline{q} - 9/4$, is

$$\frac{\partial}{\partial t_0} T_0 + \nabla_0 \cdot (\boldsymbol{v}_0 T_0) = \nabla_0^2 T_1 - w_1 \varepsilon^q, \tag{2.13a}$$

$$\frac{\partial}{\partial t_0} S_0 + \nabla_0 \cdot (\boldsymbol{v}_0 S_0) + \tau w_0 = \tau \nabla_0^2 S_1 - \tau w_1 \varepsilon^q. \tag{2.13b}$$

Subtracting these from their respective averages and using (2.9) gives

$$\frac{\partial}{\partial t_0} T_0 + \nabla_0 \cdot (\boldsymbol{v}_0 T_0) - \frac{\partial}{\partial z_0} (\overline{w_0 T_0}) = \nabla_0^2 (T_1 - \overline{T}_1) - w_1 \varepsilon^q, \tag{2.14}$$

$$\frac{\partial}{\partial t_0} S_0 + \nabla_0 \cdot (\boldsymbol{v}_0 S_0) + \tau w_0 - \frac{\partial}{\partial z_0} (\overline{w_0 S_0}) = \tau \nabla_0^2 (S_1 - \overline{S}_1) - \tau w_1 \varepsilon^q. \tag{2.15}$$

Now multiply (2.14) by τ and subtract from (2.15). The result using $T_0 = S_0$ and the vertical momentum equation is

$$(1-\tau)\left[\frac{\partial}{\partial t_0} T_0 + \nabla_0 \cdot (\boldsymbol{v}_0 T_0) - \frac{\partial}{\partial z_0} (\overline{w_0 T_0})\right] + \tau w_0 = \tau \nabla_0^2 \left(\nabla_0^2 w_0 - \frac{\partial}{\partial z_0} p_0\right). \tag{2.16}$$

Henceforth subscript zero will be dropped (all terms are leading order). From (2.11), (2.7), and the continuity equation we obtain

$$\nabla_h^2 p \equiv \frac{\partial^2}{\partial x^2} p + \frac{\partial^2}{\partial y^2} p = -\frac{\partial}{\partial z} \nabla^2 w = -\frac{\partial}{\partial z} \nabla^4 T.$$

This results in the complete system:

$$(1-\tau)\left[\frac{\partial}{\partial t} T + \nabla \cdot (\boldsymbol{v} T) - \frac{\partial}{\partial z} (\overline{w T})\right] + \tau w = \tau \nabla^6 T - \tau \frac{\partial}{\partial z} \nabla^2 p, \tag{2.17a}$$

$$\nabla_h^2 p = -\frac{\partial}{\partial z} \nabla^4 T, \tag{2.17b}$$

$$\nabla^2 u = \frac{\partial}{\partial x} p, \tag{2.17c}$$

$$\nabla^2 v = \frac{\partial}{\partial y} p, \tag{2.17d}$$

$$w = \nabla^2 T. \tag{2.17e}$$

To obtain the heat flux, temperature variance, and buoyancy flux in the same non-dimensional units as (2.3) the solution of (2.17) should be multiplied by the ε-factors listed below:

$$\langle \overline{w T'} \rangle \sim \varepsilon^2, \quad \langle \overline{T'^2} \rangle \sim \varepsilon^{3/2}, \quad \langle w(\overline{T' - S'}) \rangle \sim \varepsilon^3. \tag{2.18}$$

These important scaling laws are discussed in § 6.

In solving (2.17) using a Fourier series the typical temperature mode is

$$T = T_{k_x k_y k_z} \exp(\mathrm{i} k_x x + \mathrm{i} k_y y + \mathrm{i} k_z z) \tag{2.18a}$$

where (k_x, k_y, k_z) are the wavenumbers. From the diagnostic equations in (2.17) we then obtain the corresponding components

$$w_{k_x k_y k_z} = -\left(k_x^2 + k_y^2 + k_z^2\right) T_{k_x k_y k_z} \tag{2.18b}$$

$$p_{k_x k_y k_z} = \mathrm{i} k_z \left(k_x^2 + k_y^2\right)^{-1} \left(k_x^2 + k_y^2 + k_z^2\right)^2 T_{k_x k_y k_z} \tag{2.18c}$$

$$u_{k_x k_y k_z} = k_x k_z \left(k_x^2 + k_y^2\right)^{-1} \left(k_x^2 + k_y^2 + k_z^2\right) T_{k_x k_y k_z} \tag{2.18d}$$

$$v_{k_x k_y k_z} = k_y k_z \left(k_x^2 + k_y^2\right)^{-1} \left(k_x^2 + k_y^2 + k_z^2\right) T_{k_x k_y k_z}. \tag{2.18e}$$

We shall also need the spacially averaged downward heat flux

$$-\langle \overline{wT} \rangle = -\sum w_{k_x k_y k_z} T^*_{k_x k_y k_z} \tag{2.19}$$

where the asterisk denotes a complex conjugate and the sum is over all wavenumbers.

According to the linearized solution of (2.17) the growth rate of a single mode (2.18*a*) is

$$\lambda = \frac{\tau}{1-\tau} \left(k_x^2 + k_y^2 + k_z^2\right) \left[1 - \left(k_x^2 + k_y^2 + k_z^2\right)^2 \left(1 + \frac{k_z^2}{k_x^2 + k_y^2}\right)\right], \tag{2.20}$$

and the fastest growing (elevator) mode for $\tau = 1/3$ is given by

$$k_z = 0, \quad k_x^2 + k_y^2 = 2k^2 = 1/\sqrt{3}, \quad \tau/(1-\tau) = 1/2, \tag{2.21a}$$

$$\lambda = \lambda_1 = k^2[1 - (2k^2)^2], \tag{2.21b}$$

$$k^2 = \frac{1}{2\sqrt{3}}, \quad \lambda_1 = \frac{1}{3\sqrt{3}}. \tag{2.21c}$$

These asymptotic linear theory results converge to that for the full Navier–Stokes equations in the limit of large Prandtl number and $\varepsilon \to 0$. As previously asserted, for the same k there exists a cutoff $k_z = O(1)$ with zero growth rate, i.e. larger k_z are damped; this will appear as a significant 'slave' mode in that which follows.

3. Two-dimensional mode truncation theory

3.1. *Triad interaction equations*

The component in (2.21*a*, *b*, *c*) (called the 'elevator mode'), and a mode with the same horizontal wavenumbers but a slightly larger $k_z = m_0 \ll 1$ have essentially the same growth rate. In order to find out how the nonlinear solution of (2.17) equilibrates the latter mode, we assume it interacts with two other Fourier components: $\{k_x = k_y = k, k_z = m = O(1)\}$ and $\{k_x = k_y = 2k, k_z = \mu = m + m_0\}$. The largest scale mode with $k_x = k_y = k, k_z = m_0$ will also be denoted by the symbol $\{1, 1, 0\}$, while the other two modes are $\{2, 2, \mu\}$ and $\{1, 1, m\}$. (As already mentioned, there are many (horizontal and vertical) modes that can equilibrate the fingers and the particular horizontal wavenumbers chosen above serve only as an illustration; for the quantitative aspects of the equilibration, see the subsequent spectral solutions where all modes are present.) The nonlinear and linear terms in (2.17) with these three wavenumbers will now be collected and equated, neglecting all other Fourier components such as may arise from the product (AB) of any two scalar components (A and B). If A_{110} denotes the Fourier amplitude of mode $\{1, 1, m_0\}$ then

$$\left.\begin{aligned} &\{1, 1, m_0\} \text{ component of } AB = A_{22\mu} B^*_{11m} + B_{22\mu} A^*_{11m}, \\ &\{2, 2, \mu\} \text{ component of } AB = A_{11m} B_{110} + B_{11m} A_{110}, \\ &\{1, 1, m\} \text{ component of } AB = A_{22\mu} B^*_{110} + B_{22\mu} A^*_{110}. \end{aligned}\right\} \tag{3.1}$$

Since $w_{110} = -(2k^2 + m_0^2)T_{110}$ etc., the expansion of $\partial(wT)/\partial z$ using (3.1) with (2.18b) is

$$\left.\begin{aligned}
\frac{\partial}{\partial z}(wT)_{110} &= -\mathrm{i}m_0(10\mathrm{k}^2 + m^2 + \mu^2)T^*_{11m}T_{22\mu},\\
\frac{\partial}{\partial z}(wT)_{22\mu} &= -\mathrm{i}\mu\left(4\mathrm{k}^2 + m^2 + m_0^2\right)T_{11m}T_{110},\\
\frac{\partial}{\partial z}(wT)_{11m} &= -\mathrm{i}m\left(10\mathrm{k}^2 + \mu^2 + m_0^2\right)T^*_{110}T_{22\mu}.
\end{aligned}\right\} \tag{3.2}$$

For a plane wave disturbance with $k_y = k_x$, (2.18d, e) gives

$$\frac{\partial}{\partial x}(uT)_{110} + \frac{\partial}{\partial y}(vT)_{110} = 2\mathrm{i}\left\{\frac{\mu}{4}(8\mathrm{k}^2 + \mu^2) + \frac{m}{2}(2\mathrm{k}^2 + m^2)\right\}T_{22\mu}T^*_{11m},$$

$$\frac{\partial}{\partial x}(uT)_{22\mu} + \frac{\partial}{\partial y}(vT)_{22\mu} = 4\mathrm{i}\left\{\frac{m}{2}(2\mathrm{k}^2 + m^2) + \frac{m_0}{2}\left(2\mathrm{k}^2 + m_0^2\right)\right\}T_{11m}T_{110},$$

$$\frac{\partial}{\partial x}(uT)_{11m} + \frac{\partial}{\partial y}(vT)_{11m} = 2\mathrm{i}\left\{\frac{\mu}{4}(8\mathrm{k}^2 + \mu^2) + \frac{m_0}{2}\left(2\mathrm{k}^2 + m_0^2\right)\right\}T_{22\mu}T^*_{110}.$$

When these are inserted into (2.17a), and (2.18a–c) are used for the linear terms, we obtain

$$\dot{T}_{110} = \mathrm{i}B_1T^*_{11m}T_{22\mu} + \lambda_1T_{110}, \tag{3.3a}$$

$$\dot{T}_{22\mu} = \mathrm{i}B_2T_{11m}T_{110} + \lambda_2T_{22\mu}, \tag{3.3b}$$

$$\dot{T}_{11m} = \mathrm{i}B_3T^*_{110}T_{22\mu} + \lambda_3T_{11m}, \tag{3.3c}$$

where the overdot denotes a time derivative and

$$B_1 \equiv -\left\{\frac{\mu}{2}(8\mathrm{k}^2 + \mu^2) + m(2\mathrm{k}^2 + m^2) - m_0(10\mathrm{k}^2 + m^2 + \mu^2)\right\}, \tag{3.4a}$$

$$B_2 \equiv -\left\{2m(2\mathrm{k}^2 + m^2) + 2m_0\left(2\mathrm{k}^2 + m_0^2\right) - \mu\left(4\mathrm{k}^2 + m^2 + m_0^2\right)\right\}, \tag{3.4b}$$

$$B_3 \equiv -\left\{\frac{\mu}{2}(8\mathrm{k}^2 + \mu^2) + m_0\left(2\mathrm{k}^2 + m_0^2\right) - m\left(10\mathrm{k}^2 + \mu^2 + m_0^2\right)\right\}. \tag{3.4c}$$

The linear growth rate terms in (3.3), obtained from (2.20), are

$$\lambda_1 = \frac{1}{2}\left(2\mathrm{k}^2 + m_0^2\right)\left[1 - \left(2\mathrm{k}^2 + m_0^2\right)^2\left(1 + \frac{m_0^2}{2k^2}\right)\right], \tag{3.5a}$$

$$\lambda_2 = \frac{1}{2}(8\mathrm{k}^2 + \mu^2)\left[1 - (8\mathrm{k}^2 + \mu^2)^2\left(1 + \frac{\mu^2}{8k^2}\right)\right], \tag{3.5b}$$

$$\lambda_3 = \frac{1}{2}(2\mathrm{k}^2 + m^2)\left[1 - (2\mathrm{k}^2 + m^2)^2\left(1 + \frac{m^2}{2k^2}\right)\right], \tag{3.5c}$$

$$k^2 = \frac{1}{2\sqrt{3}}, \quad m_0 \ll 1, \quad \mu = m_0 + m. \tag{3.5d}$$

For the case when $m_0 = 0$ (elevator) we have the important inequalities

$$\lambda_1 > 0, \quad \lambda_2 < 0, \tag{3.6}$$

$$B_1 < 0, \quad B_2 = -m^3 < 0, \quad B_3 > 0, \tag{3.7}$$

In addition if m is such that

$$(2k^2+m^2)^2\left(1+\frac{m^2}{2k^2}\right)>1 \quad \text{or} \quad m>0.51, \tag{3.8a}$$

we have

$$\lambda_3<0, \tag{3.8b}$$

pointing to a range of wavenumbers m in which both $\{1,1,m\}$ and $\{2,2,m\}$ are linearly damped slave modes.

3.2. *Steady-state solutions*

Let us first note the steady solutions of (3.3) in which $\mathrm{d}/\mathrm{d}t=0$:

$$T_{22\mu}=-\frac{\mathrm{i}B_2}{\lambda_2}T_{11m}T_{110},$$

$$0=\left[\frac{B_1B_2}{\lambda_2}T_{11m}T^*_{11m}+\lambda_1\right]T_{110},$$

$$0=\left[\frac{B_2B_3}{\lambda_2}T_{110}T^*_{110}+\lambda_3\right]T_{11m}.$$

If (3.8*b*) is satisfied then we have admissible steady solutions with

$$|T_{110}|^2=-\frac{\lambda_2\lambda_3}{B_2B_3}>0 \tag{3.9a}$$

$$T_{22\mu}=\pm\mathrm{i}\sqrt{\frac{\lambda_1\lambda_3}{B_1B_3}} \tag{3.9b}$$

$$|T_{11m}|^2=-\frac{\lambda_1\lambda_2}{B_1B_2}>0. \tag{3.9c}$$

The heat flux obtained from (2.19) and (2.18*b*) is

$$-\langle wT\rangle=2\big(2k^2+m_0^2\big)|T_{110}|^2+2(8k^2+\mu^2)|T_{22\mu}|^2+2(2k^2+m^2)|T_{11m}|^2, \tag{3.10a}$$

where the factors of 2 are due to the contribution from the complex-conjugate modes.

Since k is given by (3.5*d*), the heat flux only depends on m in (3.8*a*). We conclude that the primary instability mode $k_x=k, k_y=k, k_z=m_0\to 0$ can be equilibrated by its interaction with two 'slave' modes, the crucial one $\{1,1,m\}$ being slightly (linearly) damped, according to (3.8). One particular equilibrium solution

$$|T_{110}|\sin k(x+y)+|T_{22m}|\cos[2k(x+y)+mz]+|T_{11m}|\sin(kx+mz)$$

for $m=0.8$ is plotted in figure 1(*a*).

The plot (figure 1*b*) of these steady finite-amplitude solutions for $m_0=0, \mu=m$ contains a cutoff at

$$m_c=0.51, \tag{3.10b}$$

the value of which is unchanged even if the primary mode has a small finite wavenumber $m_0\ll 1$. (A similar cutoff $m_c=0.62$ is obtained when modes $\{3/2,3/2,\mu\}$ and $\{1/2,1/2,m\}$ are chosen for the slaves and the equilibrium heat flux in this case (figure 1*c*, dashed line) is about 6 times smaller.) The physical significance of this cutoff, as revealed in figure 1(*b*), is that the energy of the equilibrating slaves is a maximum. This suggests a wavenumber (m) selection criterion similar to that used

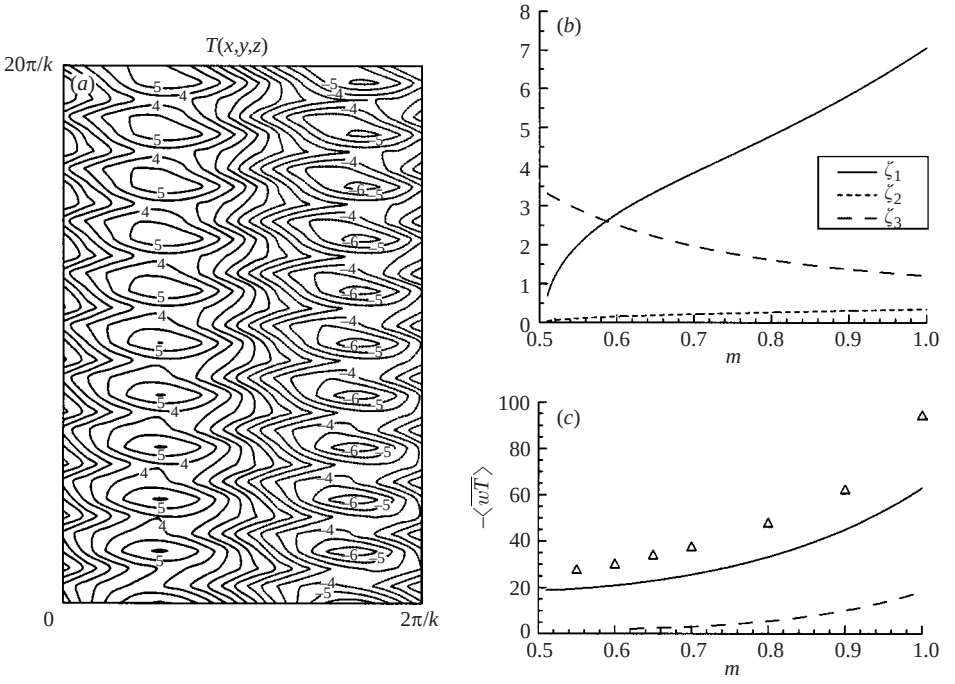

FIGURE 1. The steady solutions of (3.9) when $m_0 = 0$, $\mu = m$. (*a*) An $x = y$ cross-section of the equilibrium solution for $m = 0.8$. The horizontal domain size corresponds to one wavelength of the elevator mode ($m_0 = 0$), and the domain aspect ratio is 10:1. (*b*) $\zeta_1 = |T_{110}|$, $\zeta_2 = |T_{22m}|$, $\zeta_3 = |T_{11m}|$; the first of these is the primary finger mode which is unstable with respect to the two 'slave' modes (see text). One of these $\{1, 1, m\}$ has a maximum amplitude at the cutoff $m_c = 0.51$, and the elevator mode $\{1, 1, 0\}$ has a smaller amplitude. (*c*) The total heat flux (solid curve), however, is a minimum at m_c. No equilibrated solutions exist for $m < m_c$. The $\triangle$ points are the statistically steady values computed from the time-dependent ODE in § 3.5. The dashed curve is the flux for a smaller $k_x = k_y = k/2$ (see text).

in classical instability theory. All of the following work is directed to the question of whether m_c is realized in more complete calculations.

3.3. *Time-dependent triad interactions*

In (3.3) let

$$T_{22\mu} = -\mathrm{i}\zeta_2, \quad T_{110} = \zeta_1, \quad T_{11m} = \zeta_3. \tag{3.11}$$

If the ζ are real functions of t, then

$$\dot{\zeta}_1 = B_1\zeta_2\zeta_3 + \lambda_1\zeta_1, \tag{3.12a}$$

$$\dot{\zeta}_2 = -B_2\zeta_1\zeta_3 + \lambda_2\zeta_2, \tag{3.12b}$$

$$\dot{\zeta}_3 = B_3\zeta_1\zeta_2 + \lambda_3\zeta_3. \tag{3.12c}$$

Similar equations have been obtained previously in the context of salt fingers (Hughes & Proctor 1990) but these describe a physically different instability mechanism. We begin by considering the stability of a basic state consisting of a single amplifying finite-amplitude mode:

$$\overline{\zeta}_1 = A_1 \mathrm{e}^{\lambda_1 t}, \quad \overline{\zeta}_2 = 0, \quad \overline{\zeta}_3 = 0,$$

upon which we superimpose small perturbations ζ_1', $\zeta_2 = \zeta_2'(t)$, $\zeta_3 = \zeta_3'(t)$. The linearized evolution equations, using $\mathrm{d}/\mathrm{d}t = \lambda_1\overline{\zeta}_1\mathrm{d}/\mathrm{d}\overline{\zeta}_1$, may be written as

$$\frac{\mathrm{d}\zeta_2'}{\mathrm{d}\overline{\zeta}_1} = \frac{-B_2}{\lambda_1}\zeta_3' + \frac{\lambda_2\zeta_2'}{\lambda_1\overline{\zeta}_1},$$
$$\frac{\mathrm{d}\zeta_3'}{\mathrm{d}\overline{\zeta}_1} = \frac{B_3}{\lambda_1}\zeta_2' + \frac{\lambda_3\zeta_3'}{\lambda_1\overline{\zeta}_1}.$$

For large t and $\overline{\zeta}_1$ the last term in each of these equations is negligible, and then the asymptotic perturbation equation

$$\frac{\mathrm{d}^2\zeta_3'}{\mathrm{d}\overline{\zeta}_1^2} = \frac{-B_2B_3}{\lambda_1^2}\zeta_3' + O\left(\frac{\zeta_3'}{\overline{\zeta}_1}\right)$$

has the solution

$$\zeta_3' \simeq \exp\left[(-B_2B_3)^{1/2}\lambda_1^{-1}\mathrm{e}^{\lambda_1 t}\right],$$
$$B_2B_3 < 0.$$

Thus we see that initially the two slaves (with $m > m_c$) grow even faster (super-exponentially) than the finite-amplitude primary instability ($\overline{\zeta}_1(t)$). These theoretical results will be related qualitatively to the spectral calculations in §§4 and 5.

3.4. *Unsteady triads*

Next we consider the stability of the steady state triad $\{\overline{\zeta}_1, \overline{\zeta}_2, \overline{\zeta}_3\}$ whose finite amplitudes are given by (3.11) and (3.9), namely

$$\overline{\zeta}_1^2 = -\frac{\lambda_2\lambda_3}{B_2B_3}, \quad \overline{\zeta}_2^2 = \frac{\lambda_1\lambda_3}{B_1B_3}, \quad \overline{\zeta}_3^2 = -\frac{\lambda_1\lambda_2}{B_1B_2}. \tag{3.14}$$

If $\zeta_1'(t)$, ζ_2', $\zeta_3'\alpha\,\mathrm{e}^{\omega t}$ denote the perturbed amplitudes, then (3.12) yield the eigenvalue relation

$$\begin{vmatrix} \omega-\lambda_1 & -B_1\overline{\zeta}_3 & -B_1\overline{\zeta}_2 \\ B_2\overline{\zeta}_3 & \omega-\lambda_2 & B_2\overline{\zeta}_1 \\ -B_3\overline{\zeta}_2 & -B_3\overline{\zeta}_1 & \omega-\lambda_3 \end{vmatrix} = 0$$

for the growth rate ω. After considerable algebraic simplification utilizing (3.14) and assuming $\overline{\zeta}_1\overline{\zeta}_2\overline{\zeta}_3 > 0$, the determinant reduces to

$$\omega^3 - (\lambda_1+\lambda_2+\lambda_3)\omega^2 + 4\lambda_1\lambda_2\lambda_3 = 0. \tag{3.15}$$

The interesting case for specific discussion is near the cutoff ((3.8a, b), (3.10b)) wavenumber where $\{1, 1, m\}$ is slightly damped or

$$\lambda_3 \to 0^-, \quad \lambda_1+\lambda_2 \leqslant \frac{1}{3\sqrt{3}} - \frac{2}{\sqrt{3}} < 0. \tag{3.16}$$

We now seek asymptotic solutions of (3.15), or equivalently,

$$\omega^3 + p\omega^2 + \delta = 0$$

where

$$p \equiv -(\lambda_1+\lambda_2+\lambda_3) > 0 \quad \text{and} \quad \delta = 4\lambda_1\lambda_2\lambda_3 \to 0^+,$$

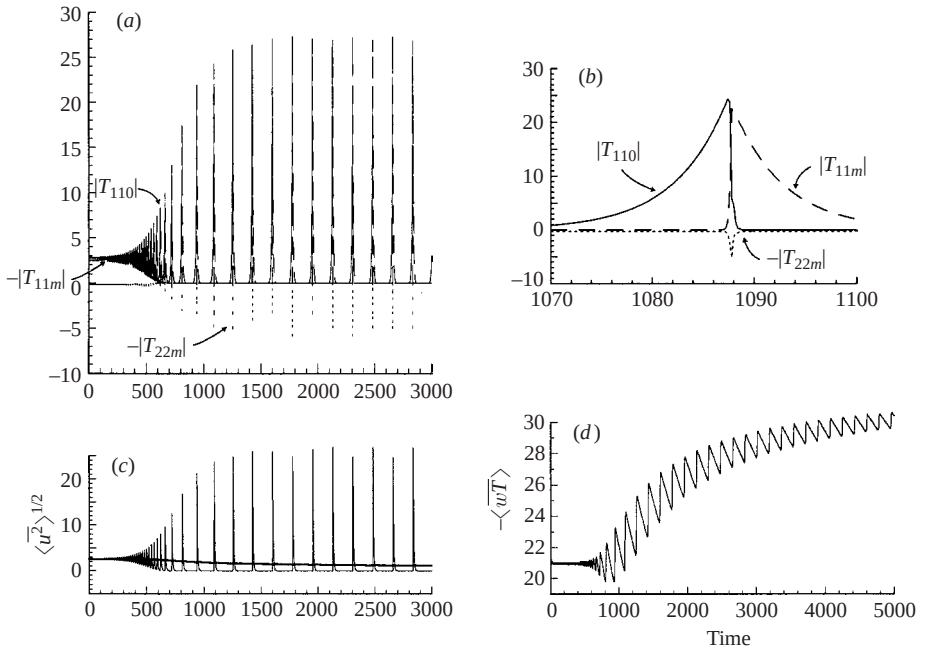

FIGURE 2. The first triad calculation for $\mu = 0.6$, $m_0 = 0$ initialized with the steady state T_{110}, T_{22m}, T_{11m}, slightly perturbed along the imaginary axis. (*a*) Time series of the T-amplitudes of the elevator mode, the primary slave mode $\{1, 1, m\}$, and the secondary slave mode $\{2, 2, \mu\}$, denoted by solid, long-dashed, and short-dashed lines, respectively. (*b*) A blow-up view of a single pulsation in (*a*). (*c*) The r.m.s. horizontal velocity (thin line) and its running average (thick line) as a function of time. (*d*) The running average of the heat flux as a function of time. The wiggles are associated with the relaxation oscillation in (*a*).

for $\omega = a\delta^{1/2} + b\delta^1 + \cdots$. From the leading- and next-order terms in the cubic expansion we obtain

$$\omega = \pm\frac{\mathrm{i}}{p^{1/2}}\delta^{1/2} + \frac{\delta}{2p^2} + \cdots,$$

$$\mathrm{Re}\,\omega \to \frac{\delta}{2p^2} > 0.$$

This shows that the steady solution with the largest slave amplitude is slightly ($O(\delta)$) amplified by an overstable oscillation with

$$\text{frequency} = -(\lambda_1 + \lambda_2)^{-1/2}(4\lambda_1\lambda_2\lambda_3)^{1/2}. \tag{3.17}$$

Therefore the strictly steady solutions cannot be realized, as demonstrated below.

3.5. *Finite-amplitude triad oscillations*

Now we turn to the time-dependent finite-amplitude solutions of (3.3) using (3.4) and (3.5) for $m_0 = 0, \mu = m$. The first calculation for $m = 0.6$ corresponds to a slightly perturbed steady equilibrium initialized with $T_{110} = 2.8 + 0.1\mathrm{i}$, $T_{22m} = -0.1\mathrm{i}$, and $T_{11m} = 2.5 + 0.1\mathrm{i}$. The ODE (3.3) was integrated in time using a second-order Runge–Kutta scheme with a time step $\Delta t = 0.01$ and double precision. The initial exponential increase in the amplitude oscillations (up to $t = 500$) on figure 2(*a*) verifies that the steady equilibrium solutions are subject to oscillatory instability (§ 3.4). The growth rate and the period of the oscillations are about 10% larger than those

predicted by (3.15), which is because the initial perturbation is not a normal mode. Despite the initial instability, the mode amplitudes and the r.m.s. horizontal velocity

$$\langle\overline{u^2}\rangle^{1/2} = \left\{\frac{m}{k}\left[\frac{8k^2+m^2}{2}\right]|T_{22m}|^2 + (2k^2+m^2)|T_{11m}|^2\right\}^{1/2}$$

seem to equilibrate at $t = 1500$ (figure 2a, c) at a periodic solution resembling a relaxation oscillator. A single relaxation oscillation is shown in detail on figure 2(b). For $1070 < t < 1086$ the primary mode ($m = 0$) grows exponentially while the two secondary modes remain of very small amplitude. Eventually, the amplitude of the primary mode becomes large and causes the super-exponential growth of the slave modes, discussed in § 3.3. As the amplitudes of the slave modes increase, the nonlinear damping ($B_1 < 0$) term in (3.3a) becomes dominant and the primary mode is rapidly damped. This in turn leads to a decrease of the nonlinear forcing terms B_2 and B_3 in (3.3b, c), and as the λ_2, λ_3 terms begin to dominate the slave modes begin to decay. Finally, when the slave mode amplitudes become very small (beyond $t > 1100$) the nonlinear damping B_1 becomes insignificant and the primary mode will grow again and the whole cycle will be repeated. Further diagnosis of the running average of the heat flux

$$\langle\overline{wT}\rangle_{RA} = \frac{1}{t}\int_0^t \langle\overline{wT}\rangle\,\mathrm{d}t'$$

(figure 2d) shows that this equilibrates at a value $\langle\overline{wT}\rangle_{RA} = -29.8$ which is roughly 50% larger than the steady-state heat flux. The running average r.m.s. horizontal velocity $\langle\overline{u^2}\rangle_{RA}^{1/2}$ (figure 2c, thick line) is, however, about 3 times smaller than the initial value. The reliability of these results was tested by repeating the calculation with halved time step $\Delta t = 0.005$. Apart from a phase lag of 1.5 time units the two calculations were identical to 4 significant digits near $t = 4953$.

The same statistical equilibrium values (to 3 significant digits) for $\langle\overline{u^2}\rangle^{1/2}$ and $\langle\overline{wT}\rangle$ were also obtained when the calculation was repeated (not shown) in the real plane by solving (3.12) in terms of the real ζ variables. Thus all subsequent calculations, exploring the dependence of the statistical equilibrium fluxes on m, will be performed in the real plane. The next such calculation (figure 3) for $m = 1.0$ is initialized with the near equilibrium values $\zeta_1 = 7.1$, $\zeta_2 = 0.35$, $\zeta_3 = 1.2$, and a time step 0.005. The early exponential instability (figure 3a, b) is again followed by nonlinear equilibration leading to a statistically steady regime for $t > 200$. Note that a much larger average heat flux $\langle\overline{wT}\rangle = -93.8$ than in figure 2(d) occurs because the latter has a much smaller temporal width for each large ζ_1 pulse.

Similar results were obtained from other calculations for values of m in the range $0.5 < m < 1.0$ and the corresponding equilibrium heat fluxes were plotted as Δ on figure 1(c). The results indicate that the equilibrium fluxes increase with m and are about 50% larger than the steady-state fluxes (figure 1c, solid line); the latter however seem to provide significant qualitative insight into the equilibration mechanism.

It is interesting to see what happens when $m = 0.5$ is below the cutoff wavenumber (m_c) for linearly damped ζ_3-modes. Initialization with $\zeta_1 = 1.0$, $\zeta_2 = 0.1$, $\zeta_3 = 3.0$ and time step $\Delta t = 0.01$ caused the primary mode ($m = 0$) to be damped (figure 4a, solid line) because the nonlinear term (B_1) overwhelms the linear amplification (λ_1). The final state was one in which only ζ_3 grows exponentially (figure 4b, c), i.e. the elevator mode gives way to the $\{1, 1, m\}$ mode which self-amplifies according to the linear theory (2.20). The same result is also obtained when the initial amplitude $\zeta_3 = 0.1$ is much smaller.

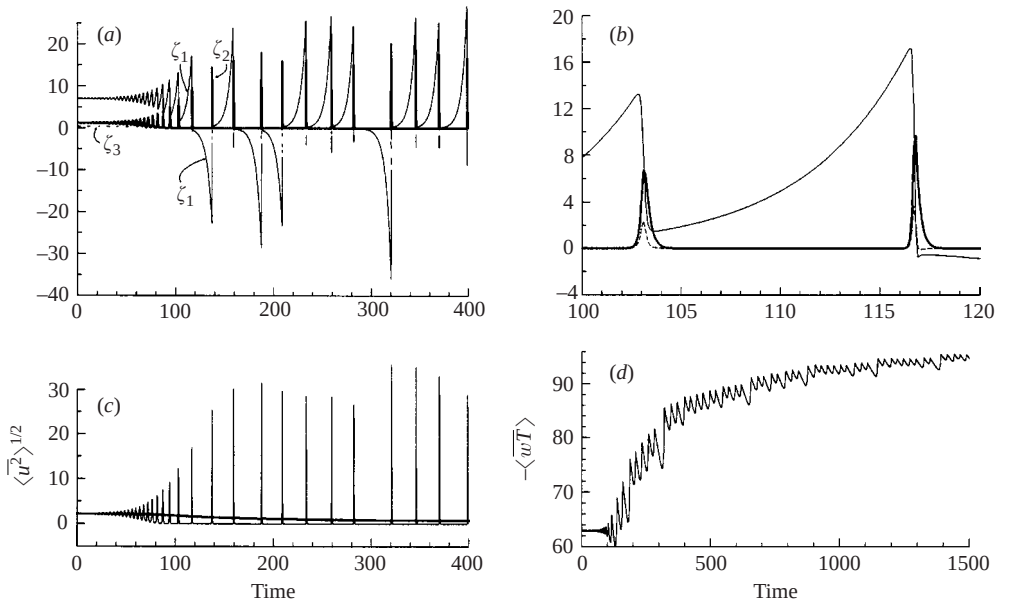

FIGURE 3. Triad calculation initialized with near equilibrium amplitudes for $m = 1.0$, and $m_0 = 0$. (*a*) Time series of the amplitudes of the elevator mode, the primary slave mode $\{1, 1, m\}$, and the secondary slave mode $\{2, 2, \mu\}$, denoted by solid, thick solid, and short-dashed lines, respectively. (*b*) A blow-up view of a single pulse in (*a*). Note the relatively short time (compared to figure 2*a*) for ζ_1 to build up to its maximum in each cycle. (*c*) The r.m.s. horizontal velocity (thin line) and its running average (thick line) as a function of time. (*d*) The running average of the heat flux as a function of time.

4. Two-dimensional spectral solutions of (2.17)

4.1. *Calculations in a narrow 1 finger-pair domain*

The foregoing results are now compared with exact two-dimensional solutions of the asymptotic equations (2.17). It is convenient, however, to rotate the axis through 45° relative to those in the preceding section, so that this two-dimensional 'roll' has vanishing y-derivative and a fundamental x-wavenumber $k_* = 3^{-1/4}$. The resulting two-dimensional equations were discretized on a 16×32 periodic grid, and therefore the solution was represented by 8 and 16 Fourier modes in the x- and z-directions respectively. The horizontal box size was set equal to the horizontal wavelength of the fastest growing elevator mode, and the vertical box size is 10 times the horizontal size. The calculation was initialized with the fundamental† mode

$$T = 0.5 \cos(k_* x) \sin(m_0 z),$$

where $m_0 = 0.1 k_*$; thus the maximum resolved vertical wavenumber is $16 m_0 \approx 1.2$, and the small random noise included wavenumber $m = 0$. A fourth-order Runge–Kutta time integration with a time step $\Delta t = 0.0001$ was used.

During the initial exponential growth (not shown in figure 5*a*) the averaged heat flux reaches a value of about -300 at $t = 23$, at which point the initial perturbation

† Although this is not the 'elevator' mode ($m = 0$), the results of § 3 for small m_0 indicate negligible difference in the heat flux.

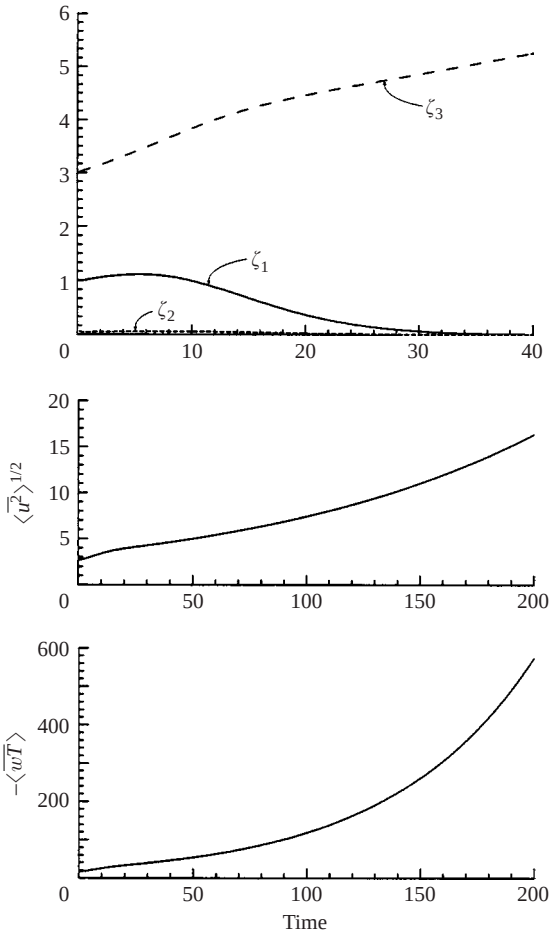

FIGURE 4. Triad calculation for $m = 0.5$ below the cutoff for steady states (figure 1). The calculation was initialized with $\zeta_1 = 1.0$, $\zeta_2 = 0.1$, $\zeta_3 = 3.0$.

starts to equilibrate via the nonlinear interaction with other modes. The subsequent variation of the averaged heat flux (figure 5*a*) indicates the eventual establishment of a statistically steady equilibrium with average heat flux $\langle \overline{wT} \rangle \approx -20$; a 20% smaller value was obtained when the calculation was repeated with double vertical resolution. Figure 5(*b*) shows typical isolines of total perturbation temperature which reveal the 'slaves' in the round eddies (compare with figure 1*a*) responsible for the equilibration of the m_0 mode. On the left and right hand sides of figure 5(*b*) there are 7–8 dominant peaks in the vertical, suggesting a vertical wavenumber $7m_0(=0.53)$ to $8m_0(=0.61)$, which agrees with the cutoff point (m_c) in the truncated calculations (§ 3); the heat flux is also comparable.

We repeated the previous calculations in a domain 5 times taller, i.e. the horizontal box size again equals the wavelength of the fastest growing elevator mode ($2\pi/k_*$), ($k_*^4 = 1/3$), but the vertical box size is 50 times the horizontal size. The calculation used 16×256 grid nodes, $\Delta t = 0.00005$, and was initialized with the fundamental z mode $T = 0.5 \cos(k_* x) \sin(m_0 z)$ where $m_0 = 0.02 k_* = 0.0152$. The maximum resolved vertical wavenumber is $128 m_0 \approx 1.95$. The statistically averaged ($100 < t < 200$) heat flux in this

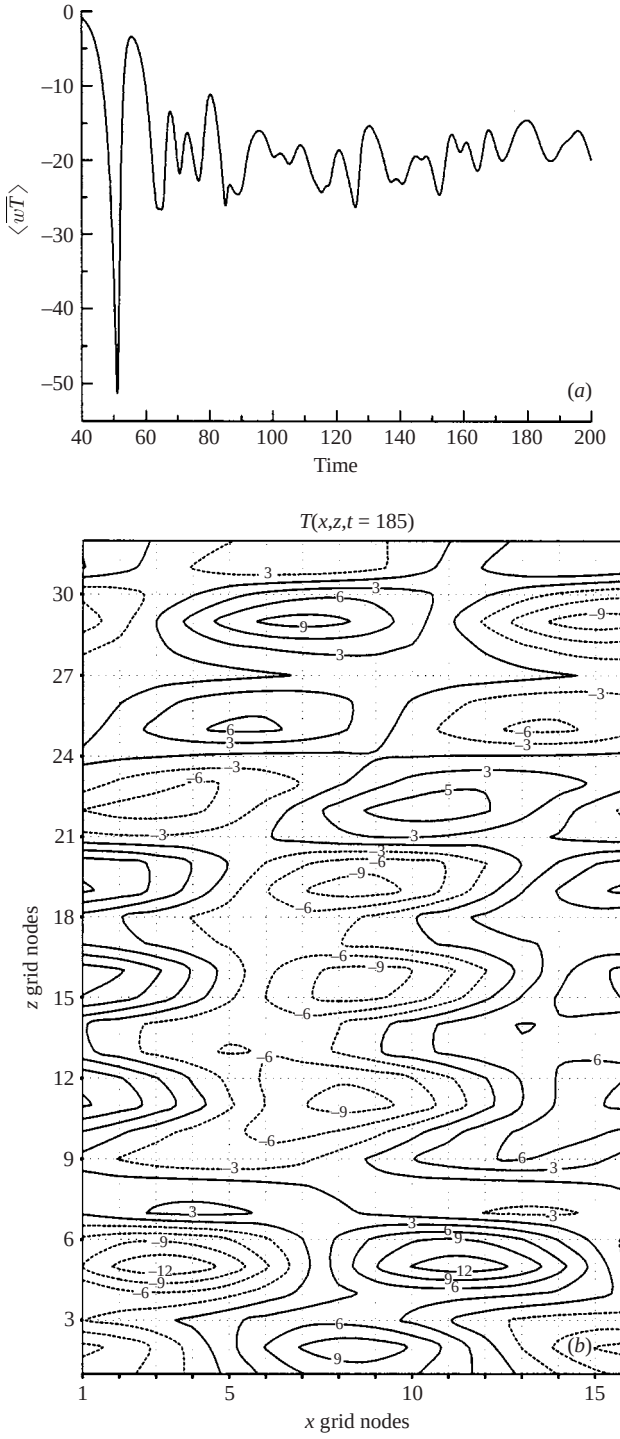

FIGURE 5. A two-dimensional spectral solution of equations (2.17) for $\tau = 1/3$, initialized with the fundamental z-mode (see text). The horizontal box size equals the wavelength of the fastest growing elevator mode and the vertical box size is 10 times the horizontal size. (*a*) Domain-averaged heat flux as a function of time. (*b*) Isotherms at $t = 185$ illustrating the slave modes.

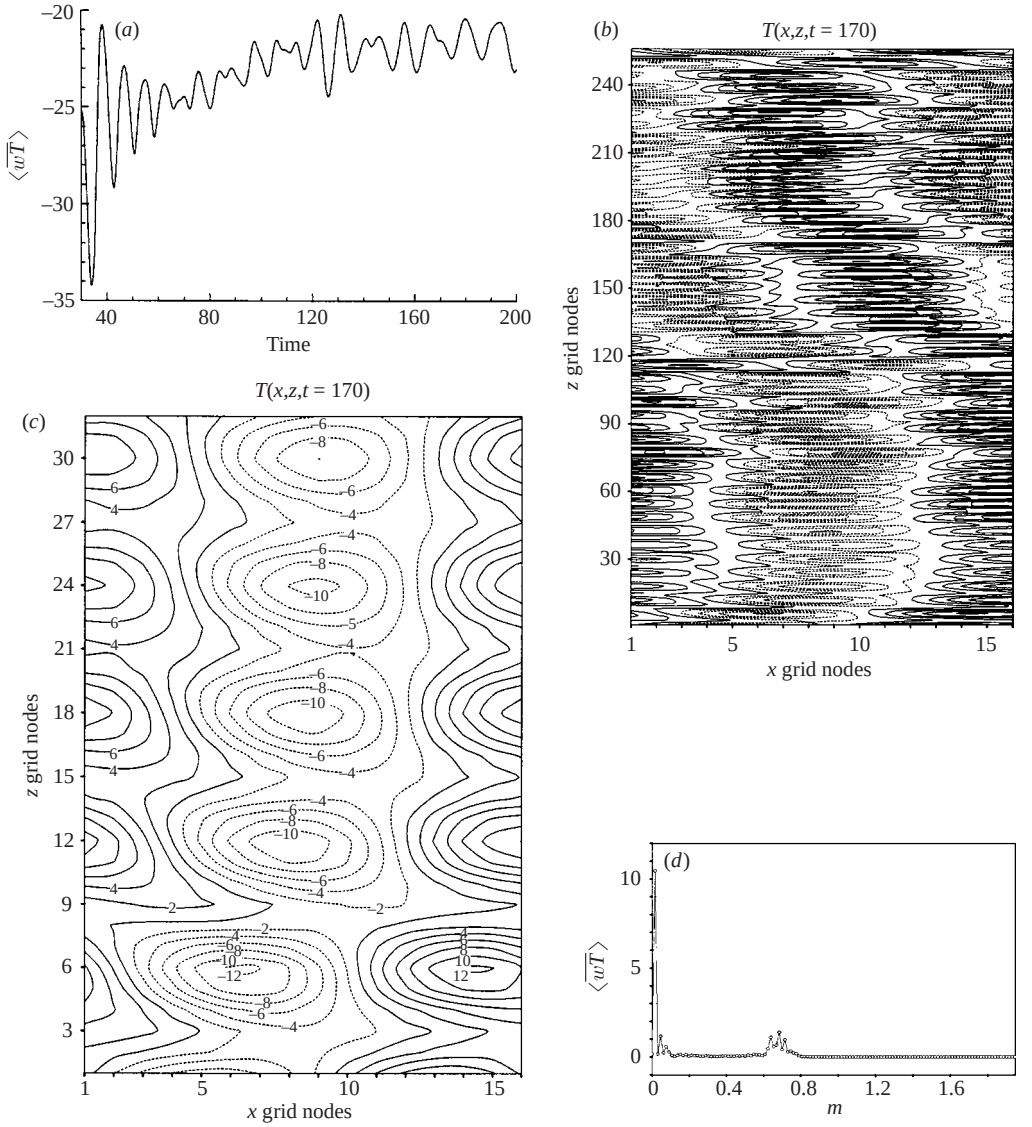

FIGURE 6. Same as figure 5 except that the vertical domain size is 5 times larger, i.e. 50 times the fastest growing wavelength. (*a*) Domain-averaged heat flux as a function of time. (*b*) Isotherms at $t = 170$ in the entire domain. (*c*) A blow-up view of the isotherms in the lower 1/8 of the domain. (*d*) Time-averaged ($50 < t < 200$) spectrum of the heat flux as a function of the vertical wavenumber; note the cutoff at $m = 0.6$.

calculation is $\langle \overline{wT} \rangle = -21.9$ (figure 6*a*), and the temperature isopleths correspond to long wavy fingers (figure 6*b*) perturbed by round eddies (figure 6*c*, a zoom of the lower 1/8 of figure 6*b*). The vertical spectrum of the heat flux (figure 6*d*) shows that the fundamental z-wavelength is responsible for almost half of the total heat flux and that there is a cutoff point at $m = 40m_0 = 0.608$ (a slightly larger value than for the previous slave eddies). The elevator mode had a negligible heat flux contribution because of the initialization used. To verify this we repeated the calculation by initializing it with the fastest growing elevator ($m = 0$) mode $T = 0.5 \sin(k_* x)$ and random noise

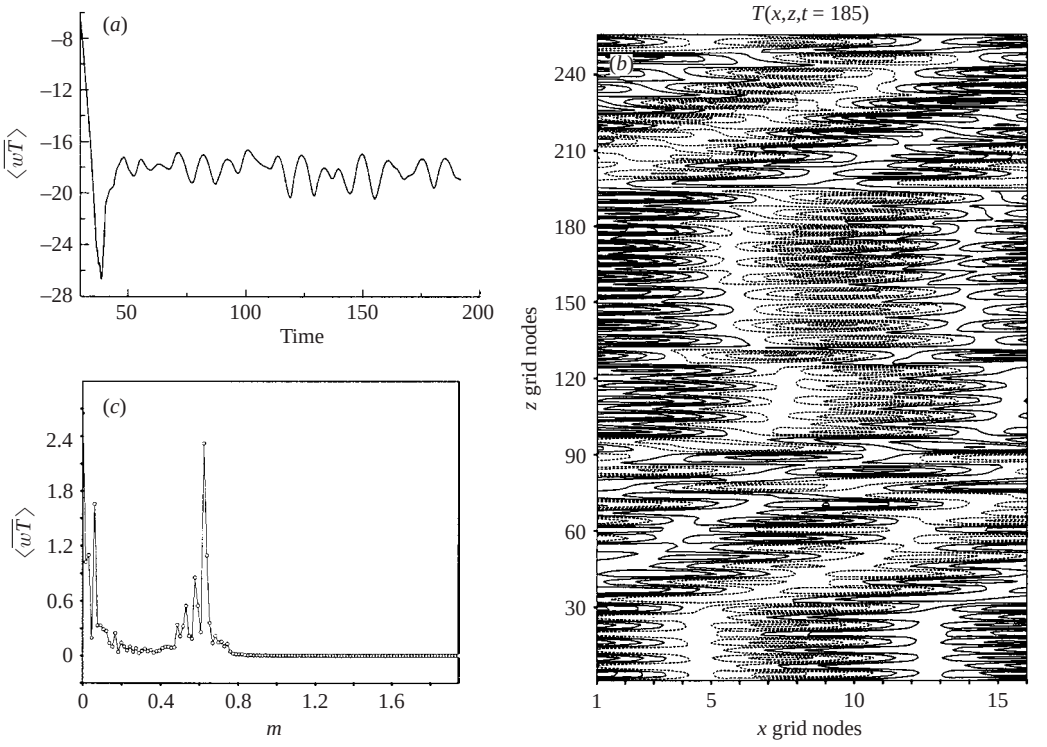

FIGURE 7. Same as figure 6 but the calculation is initialized with the elevator mode ($m = 0$). (a) Domain-averaged heat flux as a function of time. (b) Isotherms at $t = 185$ illustrating the elongated finger mode perturbed by round eddies. (c) Time-averaged ($100 < t < 190$) spectrum of the heat flux as a function of the vertical wavenumber.

of amplitude 0.025. The statistically averaged ($100 < t < 190$) heat flux in this case is $\langle \overline{wT} \rangle = -18.2$ (figure 7a) and the temperature isopleths are shown on figure 7(b). The time-averaged ($100 < t < 190$) vertical spectrum of the heat flux has a double-peak structure (figure 7c), but now the two peaks have comparable amplitudes and the elevator mode makes the maximum contribution. The heat fluxes in figures 5–7 are consistent with the cutoff steady-state solution (solid curve in figure 1c) at m_c.

4.2. *Calculations in a wide domain*

The previous section confirmed that the triad interaction mechanism of § 3 is responsible for the equilibration when the horizontal domain size is one finger wavelength. Here we increase the domain size to see if there will be any qualitative change in the equilibration mechanism.

In the first calculation we use a computational box with horizontal and vertical size set equal to 2 and 10 finger wavelengths. The resolution is the same as before (requiring 32×32 grid nodes) and the time step is $\Delta t = 0.0001$. The calculation was initialized with the fastest growing 'elevator' mode and random noise of small amplitude. A typical plot of the equilibrium isotherms (not shown) is characterized by the round eddies and is qualitatively similar to figure 5(b). There is, however, a significant quantitative difference with respect to the equilibrium heat flux $\langle wT \rangle = -3.4 \pm 0.8$ (figure 8a) which is 5 times smaller than in the case of one finger pair (figure 5a). This smaller equilibrium heat flux (compare with figure 1c dashed line) is probably

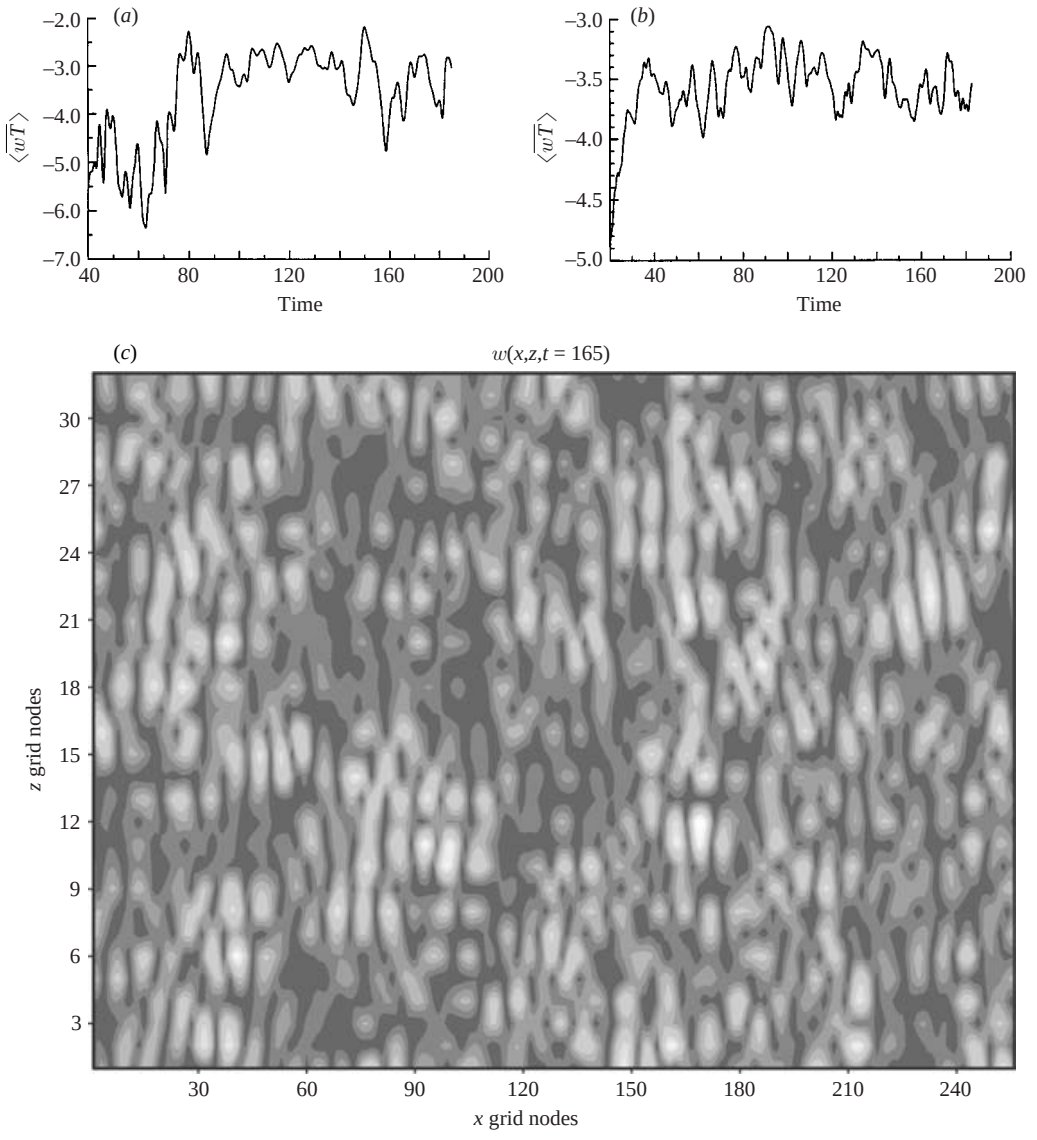

FIGURE 8(*a–c*). For caption see next page.

due to the fact that the present computational box includes triad interactions with the subharmonic mode $\{1/2, 1/2, m\}$. When this calculation was repeated in even wider domains with horizontal sizes of 8 (not shown) and 16 finger wavelengths respectively, the equilibrium heat flux was $\langle wT \rangle = -3.6 \pm 0.4$ and $\langle wT \rangle = -3.5 \pm 0.8$ (figure 8*b*). Thus an increase of the horizontal domain size beyond 2 finger wavelengths does not seem to have a further effect on the equilibrium heat flux. The isotherms in the calculation with 16 finger pairs are dominated by round eddies as in figure 5(*b*), but such a plot cannot be compared with laboratory shadowgraph images that give the variations in the index of refraction. A better comparison with the 'tree bark' shadowgraph images of Krishnamurti (2003, her figure 4), however, is obtained by plotting the magnitude of the vertical velocity (figure 8*c*) which is equal to the second derivative of the temperature. Also interesting is the average spectrum of the

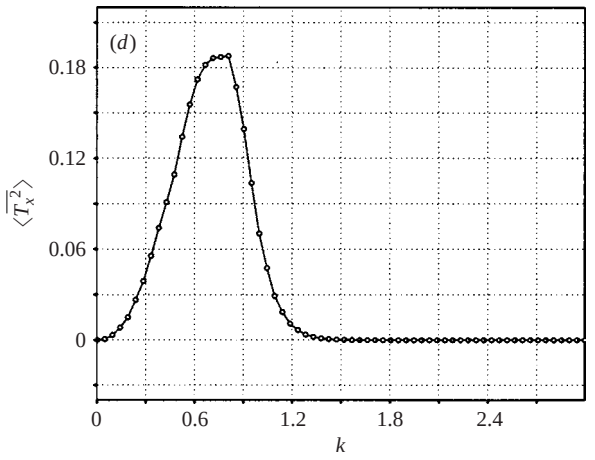

FIGURE 8. (*a*) Domain-averaged heat flux as a function of time in a two-dimensional spectral calculation which is similar to figure 5 except that the horizontal domain size is equal to 2 finger wavelengths; removed from the plot is the initial period $0 < t < 40$ when the heat flux reaches -70. (*b*) Same as (*a*) but the horizontal domain size is 16 finger wavelengths; the large heat flux peak of -74 at $t = 10.9$ has been excluded. (*c*) An x-z plot of the magnitude of the vertical velocity in the 16 finger pair calculation; the contour interval is 0.6 and the grey-scale coding is such that the maximum values correspond to white. (*d*) Time averaged ($30 < t < 200$) spectrum of the horizontal temperature gradient in the 16 finger pair calculation.

horizontal temperature gradient (figure 8*d*) which shows that for this wider domain most of the variance is still in the fastest growing wavenumber ($k = 0.76$).

5. Three-dimensional calculations for $R = 1/\tau = 3$

Radko & Stern (1999) also made preliminary three-dimensional calculations of (2.17) which showed that the two-dimensional spectral solution is unstable, resulting in much larger finger fluxes than in two-dimensions. In their calculations the domain size was $2\pi/k \times 2\pi/k \times 2\pi/m_0$, where $k = k_*/\sqrt{2}$ and $m_0 = 0.2k$ are the fundamental horizontal and vertical wavenumbers, respectively. Thus the domain was designed so that the two (fastest growing) Fourier modes with horizontal wavevectors $k_*(1/\sqrt{2}, -1/\sqrt{2})$ and $k_*(1/\sqrt{2}, 1/\sqrt{2})$ were exactly resolved on a uniform $8 \times 8 \times 32$ grid. An average three-dimensional heat flux of about $\langle \overline{wT} \rangle = -350$ was obtained. We now repeat this calculation with doubled resolution in both the horizontal and vertical ($m_0 = 0.1k_*$), i.e. $16 \times 16 \times 64$ grid nodes will be used. The initial condition (figure 9*a*) consisted of the aforementioned two Fourier modes contained in

$$T(x, y, z) = 5 \sin kx \sin ky,$$

and random noise of amplitude 10 times smaller was added. The numerical code is the same one used in Radko & Stern (1999), and time integration was performed with $\Delta t = 0.0001$. After the initial phase ($t < 10$) of linear growth the solution starts to equilibrate (figure 9*c*), and for $t > 30$ the statistically averaged heat flux $\langle \overline{wT} \rangle = -108 \pm 27$ was about 30 times larger than in our (figure 8*a*) corresponding two-dimensional run. (Approximately the same averaged heat flux $\langle \overline{wT} \rangle = -96 \pm 11$ was obtained when the calculation was repeated with doubled x, y domain sizes.) The equilibration is again due to the 'round eddies' (figure 9*d*) which extract energy from the elevator mode and dissipate it by increasing the r.m.s. vertical gradients. A typical horizontal section at $t = 190$ (figure 9*b*) illustrates the domination (and coherence) of

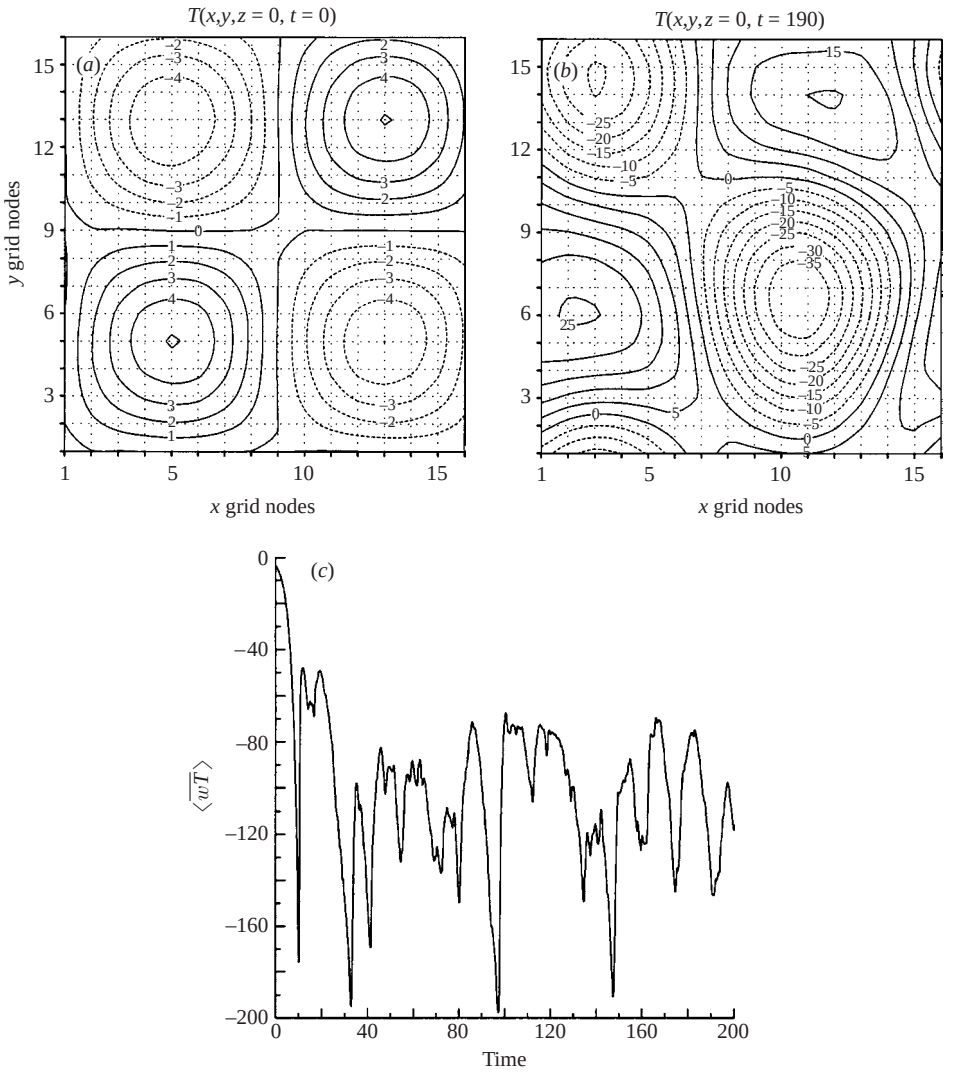

FIGURE 9(*a–c*). For caption see next page.

the two initial Fourier modes; the distortion of the latter, however, suggests that other horizontal modes are present at finite amplitude. The accuracy of the calculation was diagnosed by plotting at every 5 time units (figure 9*e*) the last three terms of the following power integral (obtained from (2.17):

$$\frac{1-\tau}{\tau}\frac{\partial}{\partial t}\left\langle\frac{\overline{T^2}}{2}\right\rangle+\langle\overline{wT}\rangle+\left\langle\overline{T\frac{\partial}{\partial z}\nabla^2 p}\right\rangle-\langle\overline{T\nabla^6 T}\rangle=0.$$

In a statistically steady state the time-derivative term vanishes and therefore the sum of the last three terms would vanish in an 'exact' calculation. In our finite-resolution calculation, however, this sum (dashed line on figure 9*e*) has a time average of about −14, which is attributed to energy losses due to the dealiasing technique (Canuto *et al.* 1987); note that the $\nabla^6 T$ term magnifies the high-wavenumber (dealiasing) errors. Compared to the energy production term $\langle\overline{wT}\rangle$ the dealiasing error is about 13%.

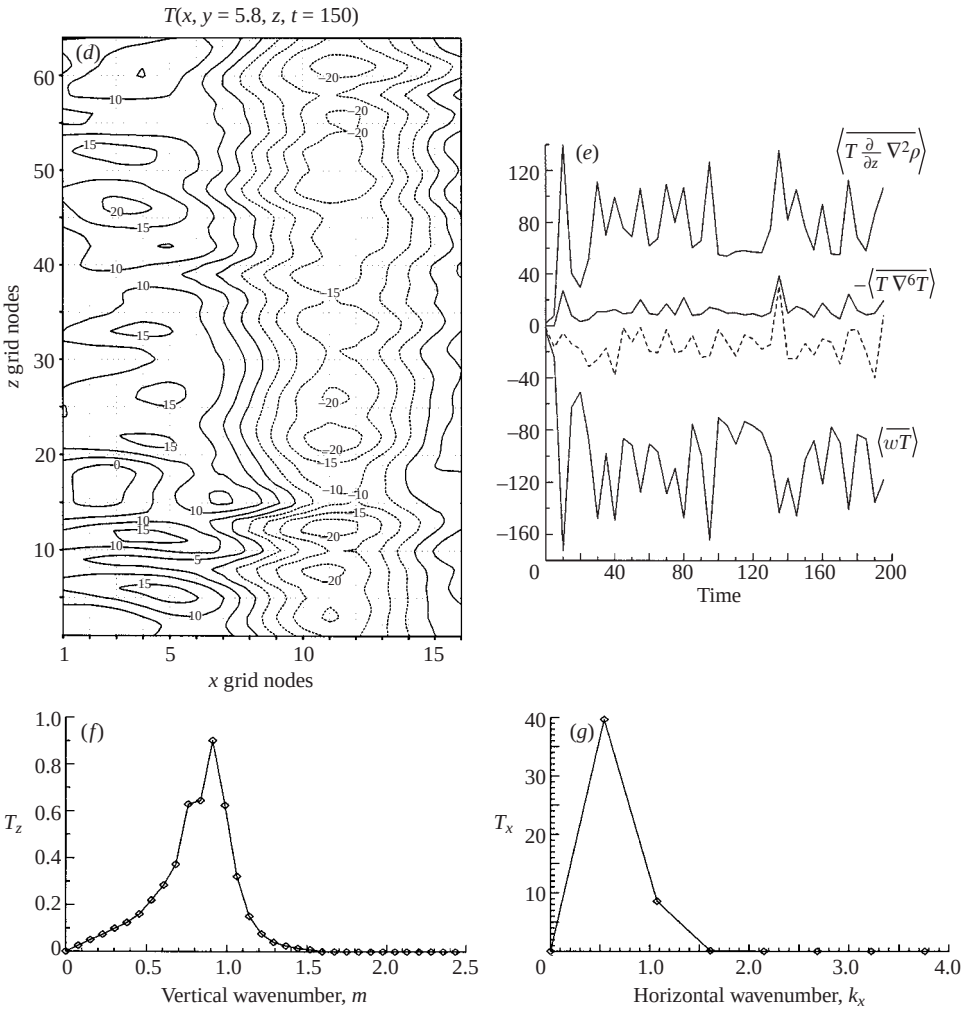

FIGURE 9. A three-dimensional spectral solution of equations (2.17) for $\tau = 1/3$, initialized with the fastest growing elevator mode with horizontal planform consisting of two 'rolls' aligned along the diagonals $x \pm y = \text{const.}$ (see text). The horizontal and vertical domain sizes are equal to $\sqrt{2}$ and 10 times the fastest growing wavelength, respectively. The grid has 16 nodes in x, y and 64 nodes in z. (*a*) Horizontal isotherm section at $z = 0$ corresponding to the initial condition. (*b*) Horizontal isotherm section illustrating the subsequent distortion of the primary mode. (*c*) Domain-averaged heat flux as a function of time. (*d*) Vertical isotherm section revealing the slave modes. (*e*) The terms in the temperature variance power integral (solid) and their sum (dashed line) as a function of time. The slight imbalance (dotted curve) is due to dealiasing errors (see text). (*f*) Time-averaged spectrum of the vertical temperature gradient as a function of the vertical wavenumber. (*g*) Time-averaged spectrum of the horizontal temperature gradient as a function of the horizontal wavenumber.

The vertical and horizontal (time-averaged) gradient spectra (figure 9*f*, *g*) indicate that our dealiased calculations have an adequate spatial resolution. As expected, the vertical gradient spectrum has a peak at $m = 12m_0 \approx 0.9$ which is somewhat in excess of the cutoff ($m_c = 0.505$) required for triad equilibration. The values of the r.m.s. gradients (the area under the spectra) are $\langle \overline{T_z^2} \rangle = 5.0$ and $\langle \overline{T_x^2} \rangle = 48.3$, respectively, and the time-averaged $\langle \overline{T_y^2} \rangle$ was only 0.4% larger than $\langle \overline{T_x^2} \rangle$.

With respect to this horizontal equipartition we briefly mention another calculation in which the numerical domain was designed to resolve exactly the resonant triad of primary Fourier modes with horizontal wavevectors $\boldsymbol{k}_1 = k_*(1, 0)$, $\boldsymbol{k}_2 = k_*(-1/2, \sqrt{3}/2)$, and $\boldsymbol{k}_3 = k_*(-1/2, -\sqrt{3}/2)$. This is achieved by setting the x and y domain sizes equal to $2\pi/(k_*/2)$ and $2\pi/(\sqrt{3}k_*/2)$, respectively. Since the grid step is a multiple of the box size it is obvious that in this case $\Delta x \neq \Delta y$. This difference, however, was minimized by using a grid with 16 nodes in x and 8 nodes in y, so that $\Delta y = (2/\sqrt{3})\Delta x \approx 1.16\Delta x$. The same vertical domain size ($m_0 = 0.1k_*$), vertical grid step, and time step as in the previous run were used. The calculation was initialized with

$$T(x, y, z) = 5\left[\sin k_* x - \sin k_* \frac{x - \sqrt{3}y}{2} - \sin k_* \frac{x + \sqrt{3}y}{2}\right],$$

which gives rise to a hexagonal horizontal pattern; random noise with 50 times smaller amplitude was added to this initial condition. Although severely distorted at times (not shown), the dominant horizontal pattern remained hexagonal as in the initial condition, but unlike the initial condition for which $\langle \overline{T_x^2} \rangle = \langle \overline{T_y^2} \rangle$ the time-averaged r.m.s. horizontal gradients were $\langle \overline{T_x^2} \rangle = 33$ and $\langle \overline{T_y^2} \rangle = 55$. The r.m.s. vertical gradient was $\langle \overline{T_z^2} \rangle = 5.9$ which is about 20% larger than in the previous run. Despite the different grid/solution geometry, the time-averaged heat flux $\langle \overline{wT} \rangle = -96 \pm 10$ was comparable to the one obtained in the previous run. We therefore conclude that, although a particular grid might bias the solution to a particular planform (squares, hexagons), the statistically averaged fluxes are independent of the grid geometry.

The reason why the three-dimensional fluxes are larger than in two-dimensions can be explained by the truncated theory (§ 3), although this pertains to a two-dimensional triad. If now an identical triad is superimposed with its axis orthogonally aligned, then the two groups are not modally coupled, and will therefore evolve independently to give a three-dimensional disturbance with a heat flux twice that of the individual triads.

6. Conclusions

Analytical and numerical calculations have been made for a density ratio (R) which is slightly less than the value ($1/\tau$) necessary to initiate long finger convection in sugar–salt solutions; the main purpose was to elucidate the mechanism by which the linearly amplifying 'elevator' mode is equilibrated. Using the Radko & Stern (1999) asymptotic theory (2.17) we first performed a two-dimensional triad mode truncation calculation. This showed that equilibration of the primary mode (the long fingers) can be accomplished by two (linearly damped) slaves, provided their vertical wavenumber exceeds 0.51 times the horizontal wavenumber of the fastest growing mode of the linear stability theory. This m_c sets the vertical 'scale' of the 'round eddies' which are found to equilibrate the amplitude in a two-dimensional spectral solution (§ 4). The mode truncation theory (§ 3) gives a good explanation of the full spectral solution, and in particular gives the mechanism of equilibration.

Three-dimensional calculations were also made and the respective values of the non-dimensional heat flux, r.m.s. vertical gradient, and r.m.s. horizontal gradients were

$$\langle \overline{wT} \rangle = -100 \pm 10,$$

$$\langle \overline{T_z^2} \rangle \cong 5.0,$$

$$\langle \overline{T_x^2} \rangle \cong \langle \overline{T_y^2} \rangle \cong 43.$$

Using the ($\varepsilon \to 0$) scaling in (2.18) the dimensional eddy diffusivity D is

$$D = K_T \left(\frac{1}{R\tau} - 1 \right)^2 \langle \overline{wT} \rangle.$$

If we make a (long) extrapolation of this result to large ε we obtain a qualitative explanation of the increase of heat flux with decreasing R as measured in heat–salt experiments (cf. Stern *et al.* 2001). Also from (2.18) we obtain a heat–salt flux ratio

$$\gamma = \frac{\langle \overline{w(T-S)} \rangle}{\langle \overline{wS} \rangle} + 1 = -\varepsilon + 1$$

which decreases from unity as R or τ decrease.

The above results are testable in sugar–salt ($\tau = 1/3$) experiments, such as performed by Krishnamurti (2003). In her figures 4 and 6 the 'lumpy' quasi-linear fingers seem to be qualitatively consistent with our triad theory and numerical calculations (figure 8*c*) since the dominant substructure consists of relatively small x- and z-wavelengths. It is especially noteworthy that the three-dimensional fluxes are thirty times the two-dimensional fluxes; in heat–salt experiments ($\tau = 1/100$) relevant to the ocean the corresponding ratio is 2 (Stern *et al.* 2001).

In conclusion, it should be noted that the self-equilibration mechanism considered here does not involve large-scale motions, e.g. external shear (Kunze 1994) or collective instability (Stern 1969). Although these other mechanisms can inhibit the fingers, they are not the primary mechanism since equilibration is possible even when they are absent. The equilibration mechanism considered here also differs from the nonlinear instability of Holyer (1984) where the triad interaction involves the marginally (zero growth) stable elevator mode, a round eddy mode, and an amplified (horizontally averaged) flow. This instability is excluded in the present large-Prandtl-number theory for which the horizontally averaged velocities vanish. The large Prandtl number also excludes the shear flow instability of Howard & Veronis (1992).

We gratefully acknowledge the support of the National Science Foundation (Grants OCE-0092504 and OCE-0236304).

REFERENCES

Canuto, C., Hussaini, M. Y., Quarteroni, A. & Zang, T. A. 1987 *Spectral Methods in Fluid Dynamics*, Springer.

Holyer, J. Y. 1984 The stability of long steady, two dimensional salt fingers. *J. Fluid Mech.* **147**, 169–185.

Howard, L. N. & Veronis, G. 1992 Stability of salt fingers with negligible diffusivity. *J. Fluid Mech.* **239**, 511–522.

Hughes, D. W. & Proctor, M. R. E. 1990 A low-order model of the shear instability of convection: Chaos and the effect of noise. *Nonlinearity* **3**, 127–153.

Krishnamurti, R. 2003 Double-diffusive transport in laboratory thermohaline staircases. *J. Fluid Mech.* **483**, 287–314.

Kunze, E. 2003 A review of oceanic salt-fingering theory. *Prog. Oceanogr.* **56**, 399–417.

Radko, T. & Stern, M. E. 1999 Salt fingers in three dimensions. *J. Mar. Res.* **57**, 471–502.

Shen, C. Y. 1995 Equilibrium salt fingering convection. *Phys. Fluids* **7**, 706–717.

Stern, M. E. 1969 Collective instability of salt fingers. *J. Fluid Mech.* **35**, 209–218.

Stern, M. E., Radko, T. & Simeonov, J. 2001 Salt fingers in an unbounded thermocline. *J. Mar. Res.* **59**, 355–390.

Stern, M. E. & Turner, J. S. 1969 Salt fingers and convecting layers. *Deep-Sea Res.* **16**, 497–511.